A pressure–velocity jump approach for the CFD modelling of permeable surfaces

(Article begins on next page)

26 November 2024

A pressure-velocity jump approach for the CFD modelling of permeable surfaces

Mao Xu[a], Luca Patruno[a,*], Stefano de Miranda[a]

[a]*DICAM, University of Bologna, Bologna, Italy*

Abstract

Permeable surfaces are extremely common in applications, ranging from wind shields installed on bridge decks to the outer layer of permeable double skin facades. However, due to the large scale separation between the overall dimensions of the structure and the size of the pores, their modelling in Computational Fluid Dynamics, CFD, simulations are still extremely problematic. In particular, explicitly modelling the pores geometry leads to prohibitive computational costs, while homogenized models based on the use of so-called pressure-jumps are often very crude simplifications of their aerodynamic behaviour. In this paper, a novel approach based on the use of pressure-velocity jumps, *PVJ*, is proposed. Firstly, the approach is deduced in a general form, based on mass and momentum conservation across the permeable surface. Then, some limit cases for which an analytical evaluation of the coefficients characterizing the model can be obtained are discussed. Finally, a ground mounted barrier is modelled, considering permeable surfaces of widely different aerodynamic behaviour. Results obtained modelling the barrier geometrical details and using the proposed *PVJ* approach are compared, confirming the soundness of the proposed approach. An OpenFOAM boundary condition implementing the proposed method is available at `https://site.unibo.it/cwe-lamc/en`.

Keywords: Computational Wind Engineering, Porous surfaces, Permeable surfaces, Pressure jump, Darcy-Forchheimer, Wind shields

1. Introduction

The use of permeable elements is extremely common in the construction industry, especially in modern architecture. When such elements are exposed to the wind action, it is necessary to quantify the aerodynamic forces to be considered for their safe design and, additionally, to consider the effect of their presence on the global aerodynamic behaviour of the structure. For instance, a typical example is represented by the presence of wind shields on bridge decks used to protect traffic against gusts: on the one side the wind action must be considered in the design of such secondary elements and, on the other side, the overall aerodynamic behaviour of the deck can be drastically changed by their presence. Recent experimental studies dedicated to the effect of wind screens on the aerodynamic performance and stability of bridge decks can be found in Kozmar et al.

---

*Corresponding author

(2014); Buljac et al. (2017). Similarly, we can mention the presence of porous screens and/or brise soleil posed in front of building facades, which might affect the local as well as the overall building aerodynamic behaviour. The wind tunnel characterization of an iconic structure located in Milan (Italy) composed of a reticular frame and porous cladding is described in Belloli et al. (2014), while studies regarding permeable facades can be found in Kemper and Feldmann (2019); Lo et al. (2020); Hu et al. (2017, 2019). Another application of interest is represented by the installation of wind barriers, often in the form of porous elements, upstream critical infrastructures in order to abate wind-blown sand transport or upstream raw material deposits to reduce dust emission. Recent experimental and numerical studies on such regard can be found, for instance, in Park and Lee (2003); Bruno et al. (2018); Raffaele et al. (2021). Further analyses on the aerodynamics of porous fences can be found, among many others, in Patton et al. (1998); Allori et al. (2013); Basnet (2015).

From the previously mentioned studies, it clearly emerges that accurately representing the flow through permeable elements is not straightforward. When considering traditional wind tunnel tests, the characteristic length scale separation between the overall structure (say 10 m) and the pores (say 0.01-0.1 m) prevents the possibility to use reduced-scale models to a large extent, unless very large testing sections are available, or rough approximations are made.

When considering CFD simulations, the same problem arises. Explicitly simulating the flow through the pores leads to prohibitive computational costs, which sum up to the already sizeable computational power usually required by Computational Wind Engineering, CWE, studies. We denote such an approach as Explicit Modelling, *EM*, in the following. In order to solve the problem, homogenized models can be used, in which the permeable surface is modelled only in terms of its effects on the flow, assuming that the pores are of vanishing size with respect to the overall structure dimensions (Xu et al., 2020). Such an approach is much more convenient with respect to *EM* both in terms of required computational resources and model setting up but, unfortunately, currently available models consider the aerodynamic behaviour of permeable surfaces in a crude and often oversimplified way.

In particular, the most widely used approach to represent thin permeable surfaces in CFD simulations is the so-called pressure-jump approach, which can be seen as an homogenized approach in which only forces acting along the normal to the permeable surface are accounted for. The approach is commonly used for internal flows (Azizi, 2019), while external aerodynamics problems have been considered for instance in Xu et al. (2022c). A typical example of pressure-jump application in the field of CWE is the modelling of permeable ground mounted barriers (Maruyama, 2008; Tominaga and Shirzadi, 2022), in which the relation between the pressure-jump and the local velocity can be obtained by means of numerical simulations on the actual barrier geometry or using empirical relations (Eckert and Pfluger, 1942; Taylor, 1944; Annand, 1953; Wieghardt, 1953). Numerical issues related to the use of pressure-jumps in the case of very low porosities have been risen in Feichtner et al. (2021), indicating that for low porosities (lower than approximately $15 - 20\%$), simulations tend to become unstable.

As already stated, in the case of pressure-jumps, the pressure field is discontinuous at the permeable surface location, being the pressure-jump equal to the drag force over the permeable surface, see for instance (Xu et al., 2022b,a). An alternative solution is to distribute the pressure

loss, i.e. the drag, over a small finite thickness. This can be achieved by considering a permeable medium, whose resistance is approximated by the Darcy-Forchheimer model (Darcy, 1856; Forchheimer, 1901). The approach thus amounts to the introduction of a distribution of properly specified negative momentum sources. For high Reynolds number flows (calculated with respect to the pore size) the inertial contribution to resistance dominates, and the viscus terms appearing in the Darcy-Forchheimer formulation can be neglected (Miguel et al., 1997; Chen and Christensen, 2016). Usually, the matrix collecting the Forchheimer coefficients is assumed to be diagonal (Yang and Lee, 1999; Cao et al., 2019) or, assuming a reference system with the first axis aligned to the permeable surface normal, only the first element on the diagonal is assumed to be non-zero. This leads to a model equivalent to the previously mentioned pressure-jump approach for porous zones of vanishing thickness (Teitel et al., 2009; Teitel, 2010).

The model can be nevertheless used with full-matrices in order to account for sharing effects. In particular such approach has been used in Ooi et al. (2019) in order to model louvers, while Pomaranzi et al. (2021) used it for the modelling of permeable stretched metal sheet. In such last case, the model has been shown to well approximate results from *EM* for angles ranging between $-45°$ and $45°$. Other examples of use of porous media can be found, for instance, in Safer et al. (2005).

In this paper, inspired by Pomaranzi et al. (2021), based on the previously cited works, we propose an extension of the pressure-jump approach, able to approximate with very good accuracy the aerodynamic behaviour of a wide range of permeable surfaces. The method is built in order to allow to accurately represent the forces exchanged between the fluid and the permeable surface at highly skew angles, considering both their component directed along the surface normal (which leads to the classical pressure-jump) and tangential direction (which leads to a velocity deflection, i.e. a jump in the tangential velocity component). As the model allows to consider both pressure and velocity jumps, it is indicated in the following as *PVJ* model. The model is devised aiming at ensuring enough flexibility to allow the representation of complex aerodynamic behaviours, without leading to an over-proliferation of tunable coefficients. Additionally, the model allows an exact representation of simple limit cases, which can be treated analytically. The soundness of the proposed approach is demonstrated by analysing ground mounted barriers characterized by widely different aerodynamic behaviours.

This paper is organized as follows. Section 2 introduces the present *PVJ* model and the limit cases which have been considered in its derivation. In Section 3, after presenting the numerical setup adopted for the numerical simulations, several permeable surfaces are analysed in periodic flow conditions, aiming at calibrating the *PVJ* model. Comparisons showing the flow fields obtained for a ground mounted barrier using explicit models and the present *PVJ* model are then reported in Section 4. Finally, conclusions are drawn in Section 5.

2. The PVJ model

Before proceeding, it is useful to summarize the desirable features that, in the authors' opinion, a model useful for the representation of permeable surfaces should have. In particular, the requirements we target are

$R1$ - approaches based on the imposition of discontinuities are preferable over distributed momentum sources, as in the latter approach the porous zone must be meshed. Inserting a thin layer of cells is problematic by itself and twice more problematic if we consider that strong gradients are expected in that zone (in the limit of vanishing permeable barrier thickness the solution is expected to be discontinuous). Such strong gradients inevitably lead to numerical errors;

$R2$ - the model shall be able to reproduce the aerodynamic behaviour of the barrier at all attack angles;

$R3$ - the model shall be flexible enough to approximate all cases of applicative interest, without leading to an uncontrolled proliferation of parameters;

$R4$ - the model should be able to reproduce exactly relevant limit cases which admit analytical solution.

In the following, for the sake of simplicity, we work on a two-dimensional model but the approach can be easily extended to three-dimensional cases, as reported in Sec. 2.3. In particular, Fig. 1 reports the scheme of an elementary portion of a permeable surface immersed in a flow characterized by velocity $\boldsymbol{u}$ and impinging with incidence angle α with respect to the barrier normal direction, $\boldsymbol{n}$.
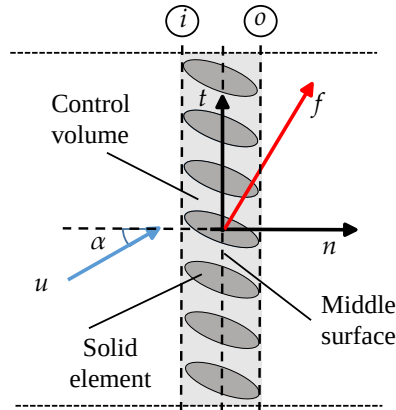

Figure 1: Sketch of a permeable surface immersed in a fluid flow.

We start assuming to know the force per unit area exerted by the fluid on the permeable surface, for all values of α, and we denote it as $\boldsymbol{f}(\alpha)$. We now consider the mass balance of the control volume bounded by the windward and the leeward surfaces of the barrier, indicated by i (i.e. incoming) and o (i.e. outgoing) in Fig. 1, respectively. Such two surfaces are depicted, for the sake of simplicity, as those bounding the permeable surface, but their actual location shall be considered to be slightly upstream and downstream, where far-upstream and downstream conditions are established (i.e. outside the zone of the flow directly affected by the pore presence). Assuming incompressibility, mass conservation requires

$$u_{ni} - u_{no} = 0, \tag{1}$$

4

where u_{ni} represents the velocity component along $\boldsymbol{n}$ measured at i, while momentum conservation in the $n-$direction requires

$$\rho(u_{ni}u_{ni} - u_{no}u_{no}) + p_i - p_o - f_n = 0. \tag{2}$$

Substituting Eq. (1) in Eq. (2), we obtain

$$p_o - p_i = -f_n, \tag{3}$$

showing that the pressure-jump measured at the two sides of the barrier is equal, and opposite, to the force acting on the barrier in the normal direction.

Analogously, momentum conservation in the $t-$direction requires

$$\rho(u_{ti}u_{ni} - u_{to}u_{no}) - f_t = 0. \tag{4}$$

Substituting Eq. (1) in Eq. (4), we obtain

$$\rho u_{ni}(u_{ti} - u_{to}) - f_t = 0, \tag{5}$$

so that

$$u_{to} - u_{ti} = -\frac{f_t}{\rho u_{ni}}, \tag{6}$$

which allows to calculate the jump of the tangential velocity component based on the exchanged forces and the mass flux across the permeable barrier.

It thus clearly appears that, in order to device a model able to represent the permeable surface, the main problem is to represent the function $\boldsymbol{f}(\alpha)$ with sufficient accuracy. Once aerodynamic forces are known, the pressure-jump is calculated according to Eq. (3), while the tangential velocity jump is obtained through Eq. (6), so allowing to satisfy requirement $R1$.

2.1. Aerodynamic forces on permeable surfaces

In this section we propose a formulation able to express $\boldsymbol{f}(\alpha)$, which comply with requirements $R2$-$R4$. We define the velocity versor as $\hat{\boldsymbol{u}} = \boldsymbol{u}/|\boldsymbol{u}|$. Then, the aerodynamic forces are assumed to be expressed by the form

$$\boldsymbol{f}(\alpha) = \frac{1}{2}\rho|\boldsymbol{u}|^2|\hat{u}_n|^\gamma \boldsymbol{c}(\alpha), \tag{7}$$

where γ is a coefficient, $|\cdot|$ denotes the $L2$ norm (or absolute value in the case of scalars) and $\boldsymbol{c}(\alpha)$ can be conveniently expressed in terms of a Fourier series as

$$\boldsymbol{c}(\alpha) = \begin{bmatrix} c_n \\ c_t \end{bmatrix} = \begin{bmatrix} b_{n0} + b_{n1}\cos(\alpha) + b_{n2}\sin(\alpha) + b_{n3}\cos(2\alpha) + b_{n4}\sin(2\alpha)... \\ b_{t0} + b_{t1}\cos(\alpha) + b_{t2}\sin(\alpha) + b_{t3}\cos(2\alpha) + b_{t4}\sin(2\alpha)... \end{bmatrix}, \tag{8}$$

in which b_{n0}, b_{t0}, b_{n1}, b_{t1}, $etc..$ are model parameters which can be obtained from data fitting or, for some limit cases, analytically. We notice that: (1) requirement $R2$ is satisfied because a Fourier series expansion is able to approximate with desired accuracy any $\boldsymbol{f}(\alpha)$ if the number of considered harmonics is increased; (2) the Fourier expansion is notoriously efficient and requires only a few harmonics to obtain good approximations, so complying with requirement $R3$.

We further notice that

- the presence of the $|\hat{u}_n|^\gamma$ term is redundant, as the Fourier expansion for $\boldsymbol{c}(\alpha)$ already allows to comply to $R2$ and $R3$. Nevertheless, such term is kept as it allows to have simpler expressions in relevant cases discussed in the following, so better complying with requirement $R4$;

- when only the first terms of Eq. (8) are kept, considering that $\hat{u}_n = \cos(\alpha)$ and $\hat{u}_t = \sin(\alpha)$ and setting $b_{n0} = b_{t0} = 0$, it is possible to rewrite the expression as

$$
\boldsymbol{c} = \left[\begin{array}{cc} b_{n1} & b_{n2} \\ b_{t1} & b_{t2} \end{array} \right] \left[\begin{array}{c} \hat{u}_n \\ \hat{u}_t \end{array} \right],
\tag{9}
$$

so leading to the linear approximation proposed for instance in Pomaranzi et al. (2021) for the momentum source term calculation.

The expressions reported in Eq. (7) and Eq. (8) simply represents one of the possible approaches which can be used to fit $\boldsymbol{f}(\alpha)$. In the following, we consider relevant limit cases which admit analytical treatment and inspired the development of the present model, so justifying the particular form selected for Eq. (7) and Eq. (8) and allowing the model to better comply with $R4$

2.2. Limit cases

In order to develop the present model, the following three limit cases have been considered, as reported in Fig. 2. In particular, we consider

LA - a flat porous sheet;

LB - largely spaced elements;

LC - a fully deflective barrier.

In all cases, we consider high Reynolds number conditions, so disregarding frictional forces.
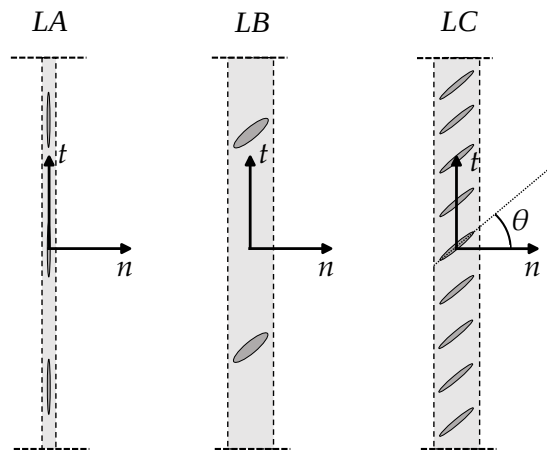

Figure 2: Limit cases considered in the definition of the proposed model: LA, flat porous sheet; LB, largely spaced elements; LC, fully deflective barrier.

2.2.1. Limit case A: flat porous sheet

The case of a flat porous sheet, indicated as LA in Fig. 2 is here considered. Due to the porous elements geometry, aerodynamic forces are exchanged only in the normal direction, so implying that c_t is null (so that, according to Eq. (6) no jump in the tangential velocity component is produced). Furthermore, the force exerted in the normal direction is usually expressed as

$$\boldsymbol{f} = \left[\begin{array}{c} \frac{1}{2}\rho k(\beta) \, |u_n| \, u_n \\ 0 \end{array} \right],$$ (10)

in which k is the so-called loss coefficient, which may be calculated as a function of the porosity β thanks to semi-analytical and empirical models (Eckert and Pfluger, 1942; Taylor, 1944; Annand, 1953; Wieghardt, 1953). Such models have been recently reviewed in Xu et al. (2020), in which a new semi-analytical model able to predict the loss coefficient based on porosity, $k(\beta)$, has been proposed.

The form reported in Eq. (10) can be obtained as a particular case of the proposed model. In fact, starting from Eq. (9) and assuming $\gamma = 1$, we have

$$\boldsymbol{f} = \frac{1}{2}\rho|\boldsymbol{u}|^2|\hat{u}_n| \left[\begin{array}{cc} k(\beta) & 0 \\ 0 & 0 \end{array} \right] \left[\begin{array}{c} \hat{u}_n \\ \hat{u}_t \end{array} \right],$$ (11)

which coincides with Eq. (10) and allows to identify $b_{n1} = k(\beta)$.

It is worth to notice that the presence of the term $|\hat{u}_n|^\gamma$ unifies two main approaches found in the literature for this limit case. In fact, the expression reported in Eq. (10) indicates a dependency of the pressure-jump on u_n^2 (implying $\gamma = 1$ in the present model). On the contrary, momentum source terms, $\boldsymbol{m}_s$, used when adopting the Darcy-Forchheimer model, are often expressed as

$$\boldsymbol{m}_s = -\frac{1}{2}\rho|\boldsymbol{u}|\boldsymbol{I}\boldsymbol{u},$$ (12)

being $\boldsymbol{I}$ the matrix containing the porous material aerodynamic resistance. As previously anticipated, such matrix is often chosen so that $I_{nn} = k/s$ where k is again the loss coefficient and s is the thickness of the porous zone created to represent the porous sheet, while all other terms are null. With such approximation, we obtain a dependency of the pressure-jump on $|\boldsymbol{u}||u_n|$ (implying $\gamma = 0$ in the present model). The results obtained by the authors in Xu et al. (2020) suggest a better performance of Eq. (10) with respect to Eq. (12), at least for the case there investigated.

2.2.2. Limit case B: largely spaced elements

Another important limit case which the model is required to reproduce exactly is that of largely spaced solid elements (see Fig. 2, LB). In this case, it is possible to assume that the local flow established around one solid element does not interact with neighboring ones, so that aerodynamic forces can be calculated for the element in isolated conditions. However, as a rough approximation in order to take into account blockage effects, it is possible to assume that the elements are immersed in a flow field in which the velocity is increased by a factor $1/\beta$ as proposed by Eckert and Pfluger (1942).

In order to reproduce such result, we impose $\gamma = 0$, so obtaining

$$\boldsymbol{f} = \frac{1}{2}\rho|\boldsymbol{u}/\beta|^2 \boldsymbol{c}(\alpha) = \frac{1}{2}\rho|\boldsymbol{u}|^2 \frac{N \cdot l_e}{\beta^2}\boldsymbol{c_e}(\alpha), \tag{13}$$

being N the number of elements per unit barrier height, $\boldsymbol{c_e}(\alpha)$ the aerodynamic coefficients of the single element calculated in isolated conditions and l_e the reference length of the single element. In the case of cylindrical elements (e.g. like wires), we can assume l_e equal to the cylinder diameter. Then, the solid area per unit area of permeable surface is $N \cdot l_e = 1 - \beta$ and we obtain

$$\boldsymbol{f} = \frac{1}{2}\rho|\boldsymbol{u}|^2 \frac{1-\beta}{\beta^2} \begin{bmatrix} C_d & 0 \\ 0 & C_d \end{bmatrix} \begin{bmatrix} \hat{u}_n \\ \hat{u}_t \end{bmatrix}, \tag{14}$$

in which C_d is the drag coefficient of the cylinder. Equation (14) allows to identify $b_{n1} = b_{t2} = C_d\frac{1-\beta}{\beta^2}$, while all other coefficient are null.

2.2.3. Limit case C: fully deflective barrier

The last limit case we analyze is that of a fully deflective barrier, indicated as LC in Fig. 2. The case consists in a porous barrier composed of lamellae which deflects the flow in the lamellae tangential direction, regardless of the impinging flow direction. In other words, lamellae are assumed to be closely spaced with respect to their length and are assumed to provide a kinematic constraint to the velocity field, so that it is forced to be tangential to the lamellae just downstream the permeable surface. We assume the lamellae to be of vanishing thickness, so that blockage effects can be neglected.
Starting from Eq. (5), substituting $u_{ti} = |u_{ni}|\tan(\alpha)$ and $u_{to} = |u_{no}|\tan(\theta)$ and accounting for mass conservation, we obtain

$$f_t = \rho u_{ni}|u_{ni}|(\tan(\alpha) - \tan(\theta)), \tag{15}$$

Dropping, for the sake of simplicity, the i pedex, such expression can be rewritten as

$$f_t = \rho|\boldsymbol{u}|^2 \hat{u}_n|\hat{u}_n| \left(\frac{\hat{u}_t}{\hat{u}_n} - \tan(\theta) \right) = \rho|\boldsymbol{u}|^2|\hat{u}_n| \left(\hat{u}_t - \tan(\theta)\hat{u}_n \right), \tag{16}$$

As the total force acting on the lamellae is constraint to be orthogonal to the lamellae (as it derives from pressure integration), we can obtain the force acting in the n direction as

$$f_n = -f_t \tan(\theta) = -\rho|\boldsymbol{u}|^2|\hat{u}_n| \left(\hat{u}_t - \tan(\theta)\hat{u}_n \right) \tan(\theta), \tag{17}$$

which can be further rewritten as

$$\boldsymbol{f} = \frac{1}{2}\rho|\boldsymbol{u}|^2|\hat{u}_n| \begin{bmatrix} 2\tan^2(\theta) & -2\tan(\theta) \\ -2\tan(\theta) & 2 \end{bmatrix} \begin{bmatrix} \hat{u}_n \\ \hat{u}_t \end{bmatrix} \tag{18}$$

so allowing to identify $\gamma = 1$, $b_{n1} = 2\tan^2(\theta)$, $b_{n2} = b_{t3} = -2\tan(\theta)$ and $b_{t3} = 2$.

8

2.3. Three-dimensional cases

The proposed model, as presented up to this point, is substantially two-dimensional. In order to extend it to three-dimensional cases, various options are available, involving different levels of approximation and expected accuracy. In the following, we assume direction r to be orthogonal to both n and t. We do not investigate full three-dimensional cases in this paper but we envisage the following possibilities, presented in order of increasing complexity

1. the permeable surface can be well-approximated by a two-dimensional model, e.g. like in the case of bars or lamellae. In this case the model already described can be readily used, although it implies that the effect of the $r-$velocity component is disregarded. The model is used preliminary projecting the velocity field along the n and t directions;

2. the permeable surface is assumed to be isotropic in the $t - r$ plane. In this case, an effective t-direction, here denoted at $\boldsymbol{t}^*$ can be identified by the versor which points in the direction of the velocity field projection over the $t - r$ plane. Then, $\boldsymbol{t}^*$ can be effectively used instead of $\boldsymbol{t}$ without further changes. This would be the preferred option for porous elements such as perforated plates and wire nets, which do not show strong anisotropy in the $t - r$ plane;

3. for general cases a complete two-dimensional Fourier expansion can be adopted instead of the mono-dimensional one presented in Eq. (8), leading to

$$\boldsymbol{f}(\alpha_1, \alpha_2) = [f_n(\alpha_1, \alpha_2), f_t(\alpha_1, \alpha_2), f_r(\alpha_1, \alpha_2)]^T. \tag{19}$$

The last solution is obviously able to represent any $\boldsymbol{f}(\alpha_1, \alpha_2)$ but remarkably complicates the model coefficients determination, which require force evaluations from numerous angles of attack. In the authors' opinion, the first two solutions shall be able to manage with good accuracy the great majority of the cases.

3. Permeable surfaces characterization

In order to apply the proposed PVJ model, firstly it is necessary to characterize the porous surface aerodynamic behaviour, i.e. the model parameters appearing in Eq. (8) must be evaluated. Such characterization is performed in Sec. 3.1 by means of CFD simulations for a representative selection of permeable surfaces, characterized by very different aerodynamic behaviours.

In the following sections, numerical simulations are performed adopting the well-known and widely adopted URANS $k - \omega\ SST$ turbulence model (Menter et al., 2003). A centered second-order differentiation scheme is adopted for the diffusive terms, while for non-linear advective terms, the Linear-Upwind Stabilised Transport (LUST) scheme is used (Weller, 2012). Time integration is performed using the Crank-Nicolson scheme and the time step is selected to make the maximum Courant number approximately equal to 1.0. The coupling of pressure and velocity is obtained using the well-known Pressure-Implicit with Splitting of Operators (PISO) algorithm. The open-source Finite Volume software OpenFOAM® v2112 is used.

3.1. Permeable surfaces

A selection of representative permeable surfaces types, characterized by very different expected aerodynamic behaviours is shown in Figure 3 (a). In particular, we consider

T1 - a surface characterized by $\beta = 0.5$ whose solid elements are equilateral triangles;

T2 - a porous surface of vanishing thickness characterized by $\beta = 0.5$, which approximates the conditions of Limit case A, LA;

T3 - a permeable surface composed of lamellae of vanishing thickness, which approximates the conditions of Limit case C, LC;

The shape of each solid element. i.e. lamella, of the *T3* case is identical to the one considered for *T2*. In order to evaluate the PVJ model coefficients appearing in Eq. (8), we perform simulations on an elementary permeable surface element in periodic conditions, considering different angles of attack as reported in Fig. 3 (b).
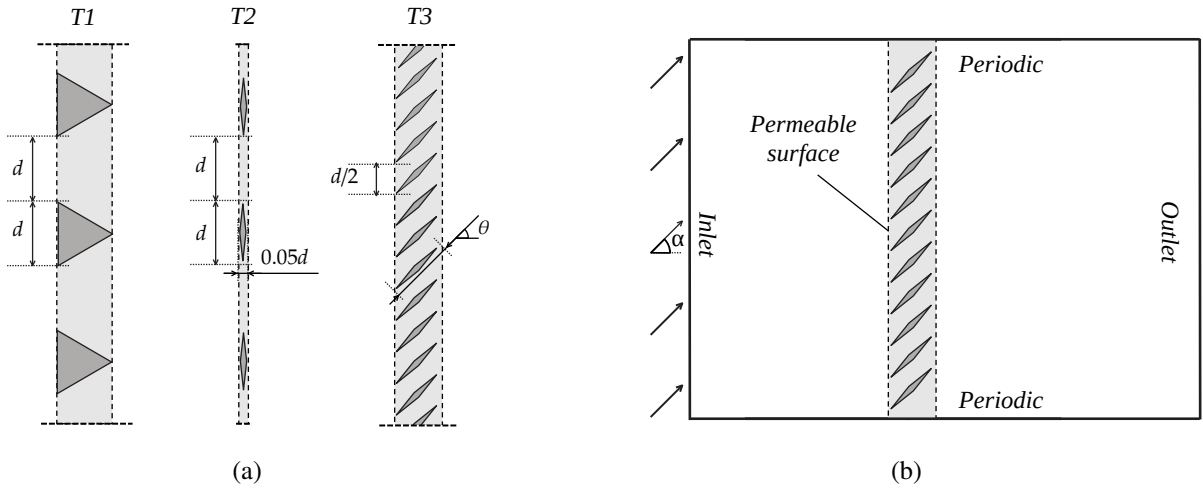

Figure 3: Porous surfaces characterization: (a) considered geometries and (b) sketch of the computational domain.

In particular, at the inlet a fixed velocity magnitude U is prescribed, with velocity components selected in order to vary the inflow angle α, together with a null pressure gradient. Periodic boundaries are adopted at the top and bottom of the domain, and a wall boundary is adopted for the solid elements composing the porous surface. A pressure outlet is adopted at the outflow. Simulations are allowed to proceed until initialization effects disappear. Then they are run for 500 non-dimensional time units tU/d, being d the characteristic dimension of the solid elements composing the permeable surface. Aerodynamic forces are extracted as the time-averaged value over the last 500 non-dimensional time units.

3.1.1. Sensitivity to mesh resolution and Reynolds number

Before proceeding, some sensitivity analysis are firstly performed. In particular, in order to check for mesh sensitivity, we start by a coarse mesh obtained discrediting each side of the solid elements using 16 cells, i.e. $N_{cell} = 16$. Then, we consider refined meshes for which $N_{cell} = 32$ and $N_{cell} = 64$, keeping all other settings the same, aiming at systematically refine the mesh in the

permeable surface proximity. Typical cell counts are in the order of $10\,k$ cells for $N_{cell} = 16$ and $100\,k$ cells for $N_{cell} = 64$. For *T1*, the obtained meshes are shown in Fig. 4.

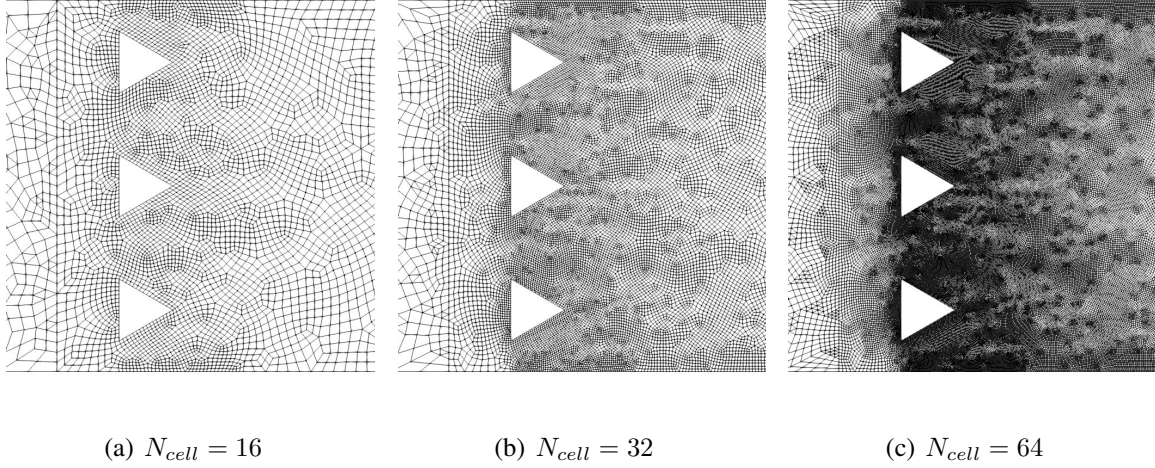(a) $N_{cell} = 16$　　　　　　(b) $N_{cell} = 32$　　　　　　(c) $N_{cell} = 64$

Figure 4: Mesh refinements used for the analysis of *T1*.

As shown in Fig. 5 (a) and (b), some differences arise in the obtained aerodynamic forces between $N_{cell} = 16$ and the others, but a very good agreement is found for $N_{cell} = 32$ and $N_{cell} = 64$, so that $N_{cell} = 32$ is kept in the following.

Next, considering again the *T1* case, we proceed to check the dependency of the obtained results on the Reynolds number based on the pore characteristic dimension, denoted as pore Reynolds number in the following, $Re_d = \frac{\rho d U}{\mu}$. This is important as we do not consider here the possibility for the model coefficients appearing in Eq. (8) to depend on the Reynolds number. Such an extension, although possible, would add considerable burden to the model calibration and, thus, for the propose of the present validation, we need to ensure that the obtained results are Reynolds independent, at least with good approximation.

Keeping the $N_{cell} = 32$ mesh, we vary Re_d in the range from 1.0×10^4 to 1.0×10^6, which well-complies with the one expected in applications and with that used in the following section. It shall be considered that in general, the local velocity is unknown and the Re_d might vary considerably between one point and the other, so that such effect might actually need consideration. Results shown in Fig. 5 show that for the *T1* case the aerodynamic forces are substantially independent from Re_d. Similar results are obtained also for the other cases, not reported for the sake of conciseness.
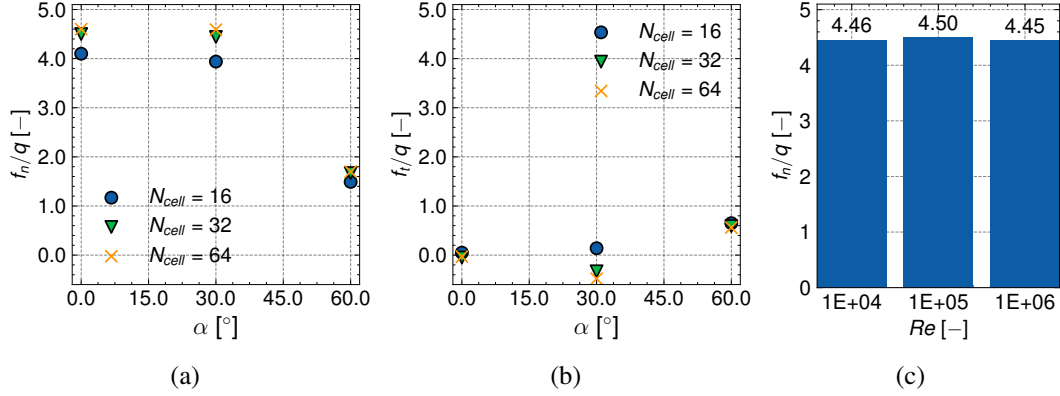
11

Figure 5: The aerodynamic coefficients: (a) f_n/q for the three different meshes, f_t/q for the three different meshes, (c) dependence on the pore Reynolds number.

3.1.2. PVJ-model calibration

Based on the previously obtained results, simulations have been performed with $N_{cell} = 32$ for all inflow attack angles, also switching the inlet and the outflow to consider angles outside the range $\alpha = [-90°, 90°]$. As an example, the velocity magnitude distribution, made non-dimensional with respect to the inflow velocity magnitude, is reported in Fig. 6 for $\alpha = 0°$ and $\alpha = 45°$.

As expected, the flow structures produced by the solid elements composing the porous surface propagate downstream for several characteristic dimensions and are then dissipated, leading to a uniform flow. In essence, the flow field across a permeable surface can be ideally subdivided into three regions: one upstream the surface in which the flow is homogeneous, a transition zone in which the flow is directly affected by the pores presence, and a zone, far downstream, in which the flow is again homogeneous. The transition zone, is usually characterized by a pressure recovery (Xu et al., 2020). When adopting homogenized models as the present PVJ one, the pores dimension is assumed to vanish, so that the far-downstream condition is established just after the permeable surface, yielding a transition zone of null thickness and, consequently, a jump from the upstream values to those expected far downstream.
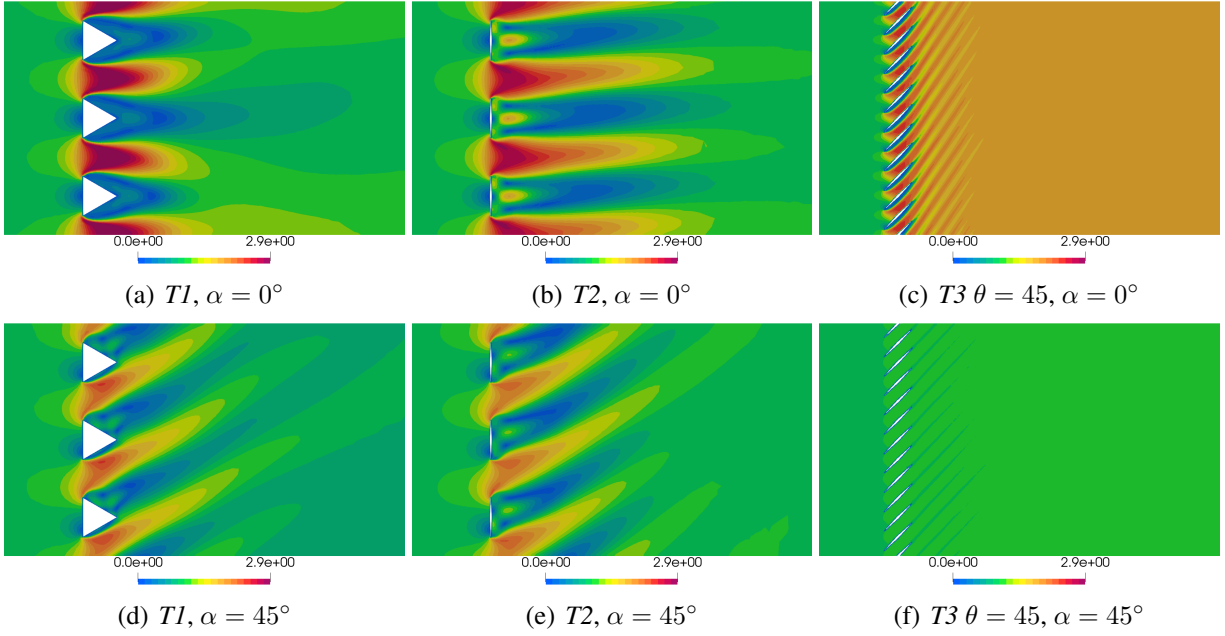
(a) *T1*, $\alpha = 0°$ (b) *T2*, $\alpha = 0°$ (c) *T3* $\theta = 45$, $\alpha = 0°$

(d) *T1*, $\alpha = 45°$ (e) *T2*, $\alpha = 45°$ (f) *T3* $\theta = 45$, $\alpha = 45°$

Figure 6: The time-averaged non-dimensional velocity magnitude, $|\bar{u}|/U$, in the permeable surface proximity with an inflow angle of $\alpha = 0°$ and $\alpha = 45°$.

Figure 7 reports the measured aerodynamic forces per unit area, $\boldsymbol{f}$, exerted form the fluid on the permeable surface, made non-dimensional with respect to $q = 1/2\rho U^2$.

(a) *T1*   (b) *T2*   (c) *T3* $\theta = 45$

(d) *T1*   (e) *T2*   (f) *T3* $\theta = 45$
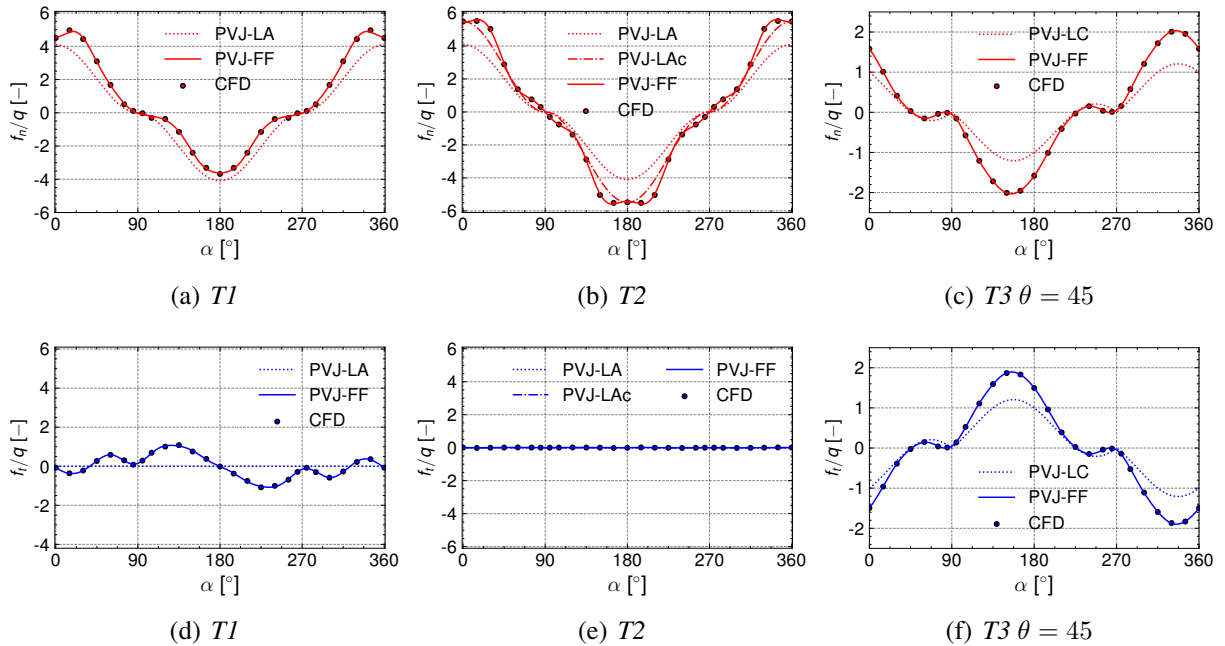
Figure 7: The non-dimensional aerodynamic forces per unit area at different angles of attack.

13

In particular, for the *T1* case reported in Fig. 7 (a) and (d), results are also compared with the semi-analytical formula proposed in Xu et al. (2020), representative of a flat porous surface of vanishing thickness (indicated as *PVJ-LA* in the following, as it provides a semi-analytical solution to the limit case LA). The formula allows to estimate the pressure-jump based on the surface porosity and thus, in this case $\beta = 0.5$ is used.

When the forces acting in the $n-$direction are compared, see Fig. 7 (a), the formula provides good agreement with the numerical results, despite being obtained for a quite different and simpler case. When the forces acting in the $t-$direction are considered, see Fig. 7 (b), *PVJ-LA* leads to null values while, as expected, non-zero values are obtained from the numerical model. Finally, a fitting of Eq. (8) considering 9 harmonics is reported as *PVJ-FF*. In this last case, γ can be arbitrarily set to a null value (as it is redundant) and expectedly, a very good fitting is obtained.

For the *T2* case, reported in Fig. 7 (b) and (e), results from the numerical simulations are again compared to *PVJ-LA*, still considering $\beta = 0.5$. In this case, the hypotheses leading to the development of the semi-analytical formula reported in Xu et al. (2020) are well-met (flat porous surface of vanishing thickness) but, despite the good qualitative agreement in terms of trends, *PVJ-LA* predicts a lower force in the $n-$direction with respect to the measured one. This must be attributed to the fact that the flow detaches at the solid elements edges, leading to a vein contraction which reduces the effective aerodynamic porosity with respect to the geometrical one. Reducing the porosity of approximately 10% (i.e. assuming $\beta = 0.45$) we obtain the results indicated as *PVJ-LAc*, which show a very good agreement with the numerical simulations. Alternatively, a fitting of the obtained data using Eq. (8) can be obtained, indicated as *PVJ-FF*.

Finally, we consider the case denoted as *T3* $\theta = 45$, reported in Fig. 7 (c) and (f). In this case, together with the simulation results, we show the prediction of Eq. (18), indicated as *PVJ-LC*, as it provides a solution to the limit case LC. In this case, for both the $n-$ and $t-$directed forces, *PVJ-LC* is lower than the prediction of the numerical simulations, despite the fact that trends are correctly captured. It can be seen that such discrepancy is originated by the generation of separation bubbles on one side of the lamellae, which lead to a modification of the lamellae effective geometry and, thus, a higher-than-expected deflection angle, i.e. the velocity downstream the lamellae is not aligned to the lamellae. Actually, a very good matching of the numerical results can be obtained multiplying *PVJ-LC* by a factor 1.5 (not shown for the sake of brevity) or, proceeding by mere fitting of the numerical results by means of Eq. (8), indicated again as *PVJ-FF*.

In summary, the coefficients appearing in Eq. (8) can be always tuned in order to match numerical or experimental results. Quantitative mismatches with respect to the limit cases presented in Sec. 2.2 shall be expected due to aerodynamic effects (i.e. vein contraction, generation of separation bubbles in proximity of the lamellae) which makes it difficult to uniquely characterize the aerodynamic behaviour based on the permeable surface geometry only. However, limit cases provide good guidance for results interpretation and *a priori* evaluations.

4. Results

In this section, we proceed to the comparison of the results obtained using *EM* and *PVJ* for the simulation of a ground mounted permeable barrier. Firstly, the case is introduced in Sec. 4.1, and the dependency of the results on the number of solid elements composing the barrier is assessed.

Then, *EM* and *PVJ* approaches are compared for the permeable surfaces types characterized in Sec. 3.1.

4.1. Case geometry and sensitivity to scale separation

A sketch of the considered ground mounted permeable barrier is reported in Fig. 8 (a). In particular, we consider a permeable barrier of height H immersed in a uniform flow. The ground is modelled as a wall-boundary condition, while symmetry is used for the upper boundary condition. Other geometrical details of the adopted computational setup are reported in Fig. 8 (a), while numerical settings are the same previously described in Sec. 3.

The proposed *PVJ* approach is expected to approach *EM*, only if the size of the elements composing the porous surface vanishes with respect to the overall studied object size or, in other terms, if a good scale separation between the pore size and the barrier size is reached. To check for scale-separation effects, keeping H constant, the number, N_o, of solid elements (i.e. triangles in this case, see Fig. 8 (b) and (c)) is varied from $N_o = 10$ to $N_o = 25$, so consequently decreasing their size. The operation is performed keeping the number of cells used to discretize each side of the triangles equal to $N_{cell} = 32$, in agreement with the previously found results. The operation is repeated considering $N_o = 10, \ 25, \ 50$ and 75. Typical cell counts are in the order of $100k$ cells for $N_o = 10$ and $400k$ cells for $N_o = 50$. Notice that, beside the previously introduced pore Reynolds number Re_d, a Reynolds number based on the barrier height, Re_H, can be introduced. For the present case Re_H is fixed as H is the same for all analyses, but Re_d varies between 3.0×10^5 to 4.0×10^4, when considering increasing N_o. However, within such range, results have been shown to be substantially insensitive to Re_d in Sec. 3.1.1.
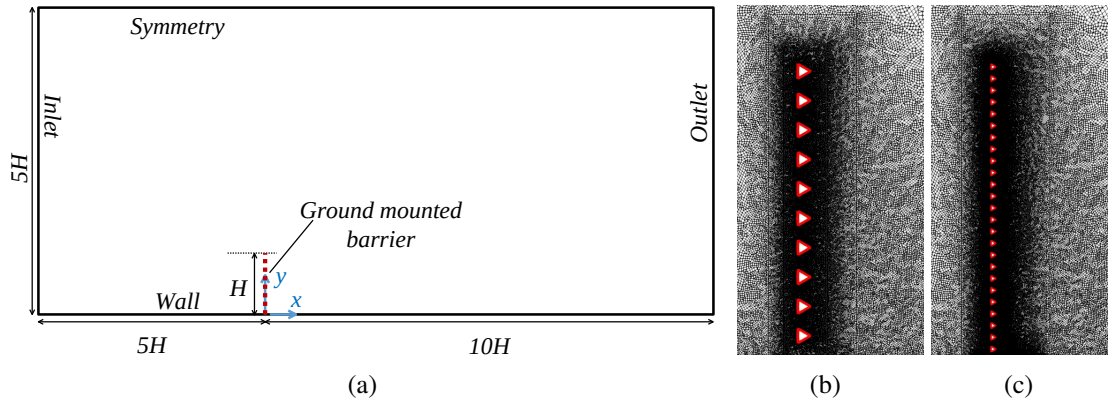

Figure 8: The considered ground-mounted permeable barrier: (a) case geometry, (b) *T1* with $N_o = 10$ and (c) *T1* with $N_o = 25$.

The results obtained varying N_o are reported in Fig. 9 for two radically different cases: *T3* $\theta = 45$ and *T3* $\theta = -45$. It can be clearly seen that, as expected, the orientation of the lamellae has a very strong effect on the overall flow field organization and that results obtained with different N_o are in good agreement with each other, being $N_o = 50$ and $N_o = 75$ hardly distinguishable. Similar results have been obtained for the other permeable surfaces analysed in Sec. 3.1.2, which are not reported for the sake of brevity (the measured global forces are nevertheless reported for

all cases at the end Sec. 4.2). Considering that results obtained with $N_o = 10$ and 25 show visible, although small, differences with respect to the others, we proceed in the following with $N_o = 50$.
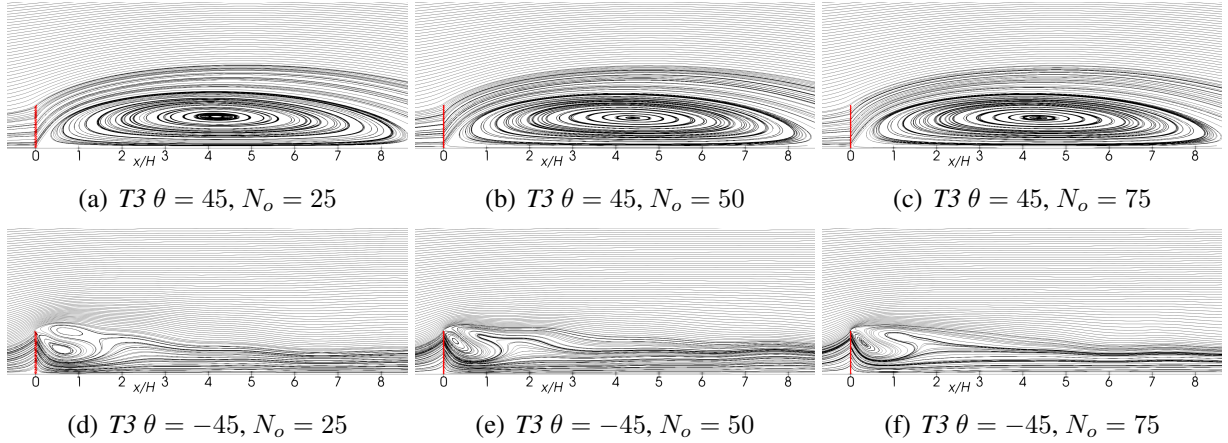

(a) *T3* $\theta = 45$, $N_o = 25$ (b) *T3* $\theta = 45$, $N_o = 50$ (c) *T3* $\theta = 45$, $N_o = 75$

(d) *T3* $\theta = -45$, $N_o = 25$ (e) *T3* $\theta = -45$, $N_o = 50$ (f) *T3* $\theta = -45$, $N_o = 75$

Figure 9: The streamlines of the time-averaged flow of the *EM* models with different N_o.

4.2. Comparison between EM and PVJ

We now proceed at comparing the results obtained by using *EM* and *PVJ* approaches. In particular, Fig. 10 (a) reports the streamlines obtained considering the *EM* model for the *T1* case, while Fig. 10 (b) and (c) show the streamlines obtained using *PVJ* considering the limit case *PVJ-LA* (see Sec. 3.1.2) and data fitting, indicated as *PVJ-FF*. It can be seen that a good qualitative agreement is obtained between all cases. Notice again that *PVJ-LA* is expected to be only a crude approximation of the *T1* case, but a very good agreement is actually obtained, so justifying the use of simple pressure-jumps for such case.
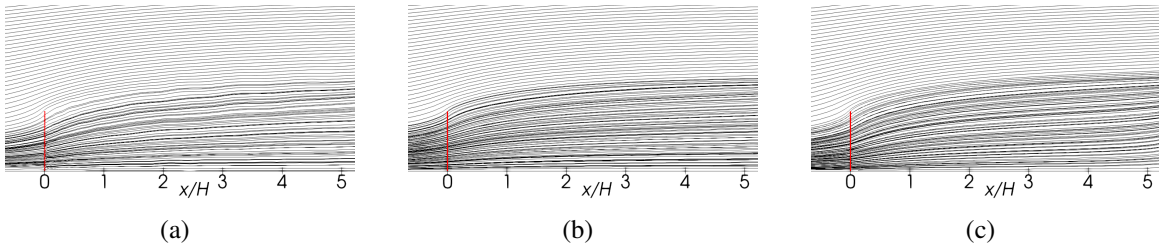

(a)   (b)   (c)

Figure 10: The streamlines of the time-averaged velocity field for the *T1* case: (a) *EM*, $N_o = 50$, (b) *PVJ-LA*, $\beta = 0.5$ and (c) *PVJ-FF*.

Analogously, Fig. 11 reports the comparison between *EM* and *PVJ* approaches for the *T2* case. Notice that the *PVJ-LA* case is identical to that already presented for *T1* in Fig. 10 (b). Also in this case, the agreement between the three cases is very good, highlighting that *PVJ-LA* provides a very good approximation of the barrier aerodynamic behaviour, as expected.
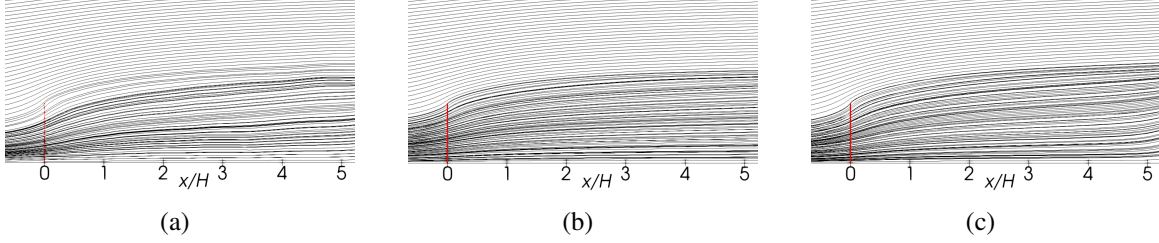
Figure 11: The streamlines of the time-averaged velocity field for the *T2* case: (a) *EM*, $N_o = 50$, (b) *PVJ-LA*, $\beta = 0.5$ and (c) *PVJ-FF*.

In the previous examples, the main effect induced by the permeable barrier was the generation of a pressure-jump. We now consider the *T3* $\theta = 45$ case, which induces also a strong velocity deflection. Figure 12 reports the streamlines obtained adopting the *EM* and the *PVJ* models, together with *PVJ-LC* as limit case. The obtained results are substantially different from those obtained for *T1* and *T2*, with a vortex developing downstream the barrier. Reasonable qualitative agreement is again obtained between all three models, with *EM* and *PVJ-FF* in very good agreement.
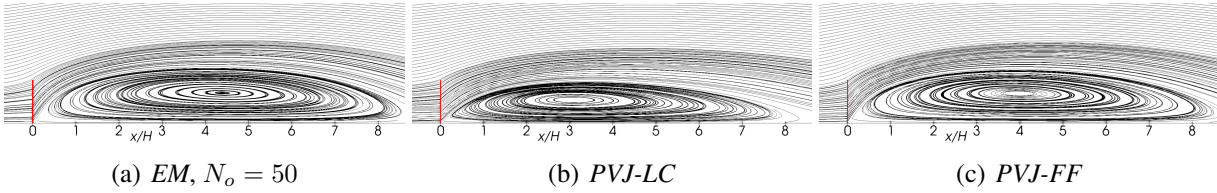

(a) *EM*, $N_o = 50$ (b) *PVJ-LC*   (c) *PVJ-FF*

Figure 12: The streamlines of the time-averaged velocity field for the *T3* $\theta = 45$ case: (a) *EM*, (b) *PVJ-LC* and (c) *PVJ-FF*.

Finally, in Fig. 13, we consider the case *T3* $\theta = -45$, which can be obtained still relying on the same PVJ parameters used for *T3* $\theta = 45$ just switching the $t-$direction, showing again good agreement between *EM* and *PVJ*. In this case, the flow does not converge to a stationary solution so, for the sake of completeness, streamlines of the instantaneous velocity field are reported in Fig. 14. In particular, for the sake of comparability, streamlines are reported for all considered models considering an instant in which a crest in the streamlines is present at the location $x/H = 4.5$. The similarity between the obtained flow fields is again confirmed.
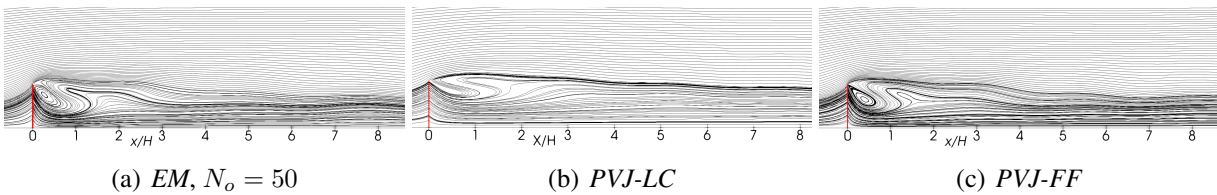

(a) *EM*, $N_o = 50$ (b) *PVJ-LC*   (c) *PVJ-FF*

Figure 13: The streamlines of the time-averaged velocity field for the *T3* $\theta = -45$ case: (a) *EM*, (b) *PVJ-LC* and (c) *PVJ-FF*.

17

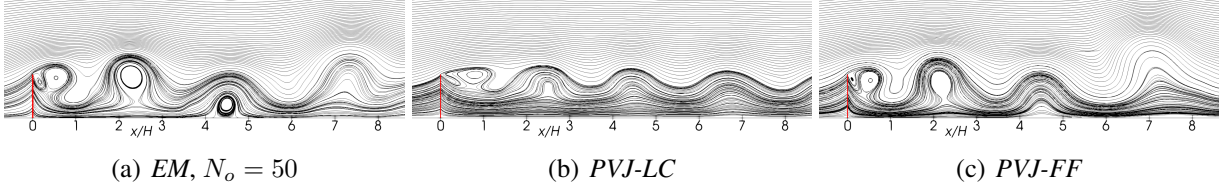(a) *EM*, $N_o = 50$ (b) *PVJ-LC*   (c) *PVJ-FF*

Figure 14: The streamlines of the instantaneous velocity field for the *T3* $\theta = -45$ case: (a) *EM*, (b) *PVJ-LC* and (c) *PVJ-FF*

In order to provide a more quantitative inspection of the obtained results, Figs. 15-18 report the vertical profile of the time-averaged velocity component along the x-direction, $\overline{u}_x$, downstream the porous barrier at $x/H = 0.5, \ 1.0, \ 4.0$. The good qualitative agreement previously observed is here again confirmed.
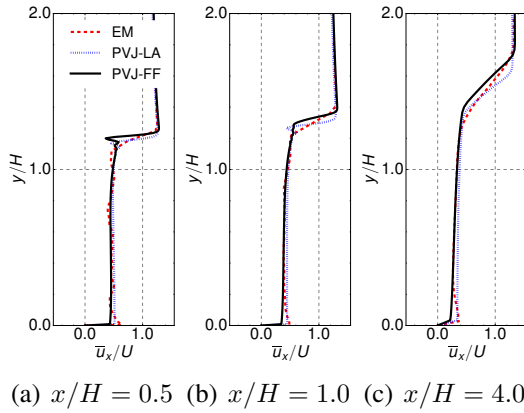

(a) $x/H = 0.5$ (b) $x/H = 1.0$ (c) $x/H = 4.0$

Figure 15: The vertical profiles of the time-averaged velocity component along x, $\overline{u}_x/U$, for *T1*.

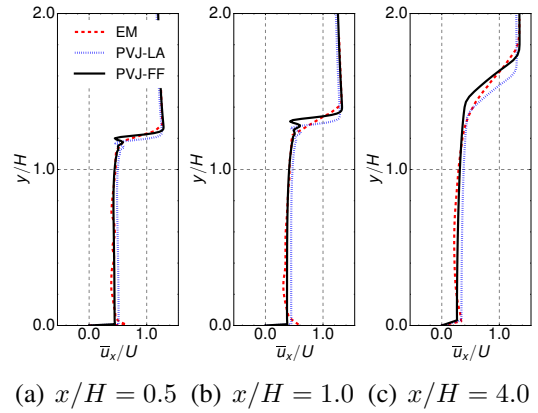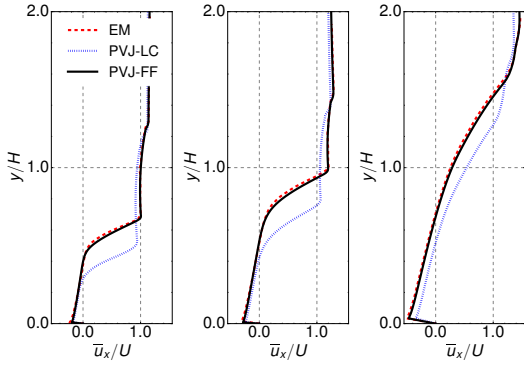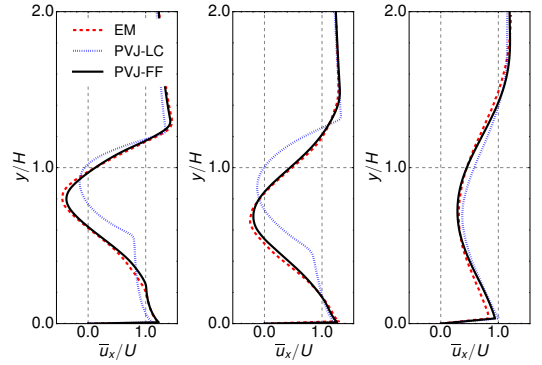(a) $x/H = 0.5$ (b) $x/H = 1.0$ (c) $x/H = 4.0$

Figure 16: The vertical profiles of the time-averaged velocity component along x, $\overline{u}_x/U$, for *T2*.
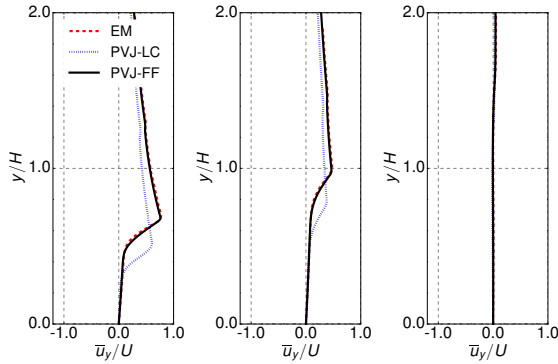
(a) $x/H = 0.5$ (b) $x/H = 1.0$ (c) $x/H = 4.0$

Figure 17: The vertical profiles of the time-averaged velocity component along x, $\overline{u}_x/U$, for *T3* $\theta = 45$.

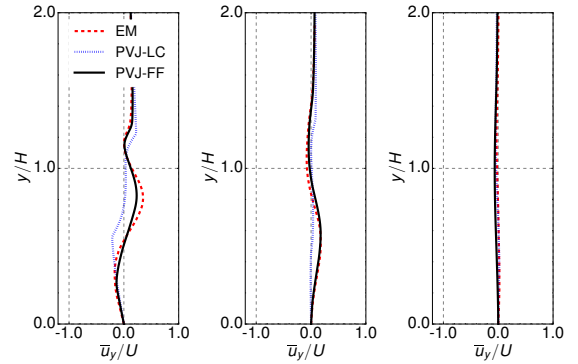(a) $x/H = 0.5$ (b) $x/H = 1.0$ (c) $x/H = 4.0$

Figure 18: The vertical profiles of the time-averaged velocity component along x, $\overline{u}_x/U$, for *T3* $\theta = -45$ case.

For the sake of completeness, for *T3* $\theta = 45$ and *T3* $\theta = -45$, which are characterized by the strongest velocity deflections, vertical profiles of the time-averaged velocity component along the y-direction, $\overline{u}_y$, are also reported in Figs. 19-20.

(a) $x/H = 0.5$ (b) $x/H = 1.0$ (c) $x/H = 4.0$

Figure 19: The vertical profiles of the time-averaged velocity component along y, $\overline{u}_y/U$, for *T3* $\theta = 45$.

(a) $x/H = 0.5$ (b) $x/H = 1.0$ (c) $x/H = 4.0$

Figure 20: The vertical profiles of the time-averaged velocity component along y, $\overline{u}_y/U$, for *T3* $\theta = -45$.

Finally, global aerodynamic coefficients representative of the forces acting on the barrier along the $x-$direction and $y-$direction are reported in Fig. 21. In particular, we define $C_i = F_i/qH$ with $i = x, y$ and $q = 1/2\rho U^2$. In this case, together with the results obtained adopting *PVJ*, we report results obtained with *EM* using different N_o. In particular, it clearly appears that increasing N_o leads to a convergence of the obtained result toward those obtained using *PVJ-FF*, as expected.
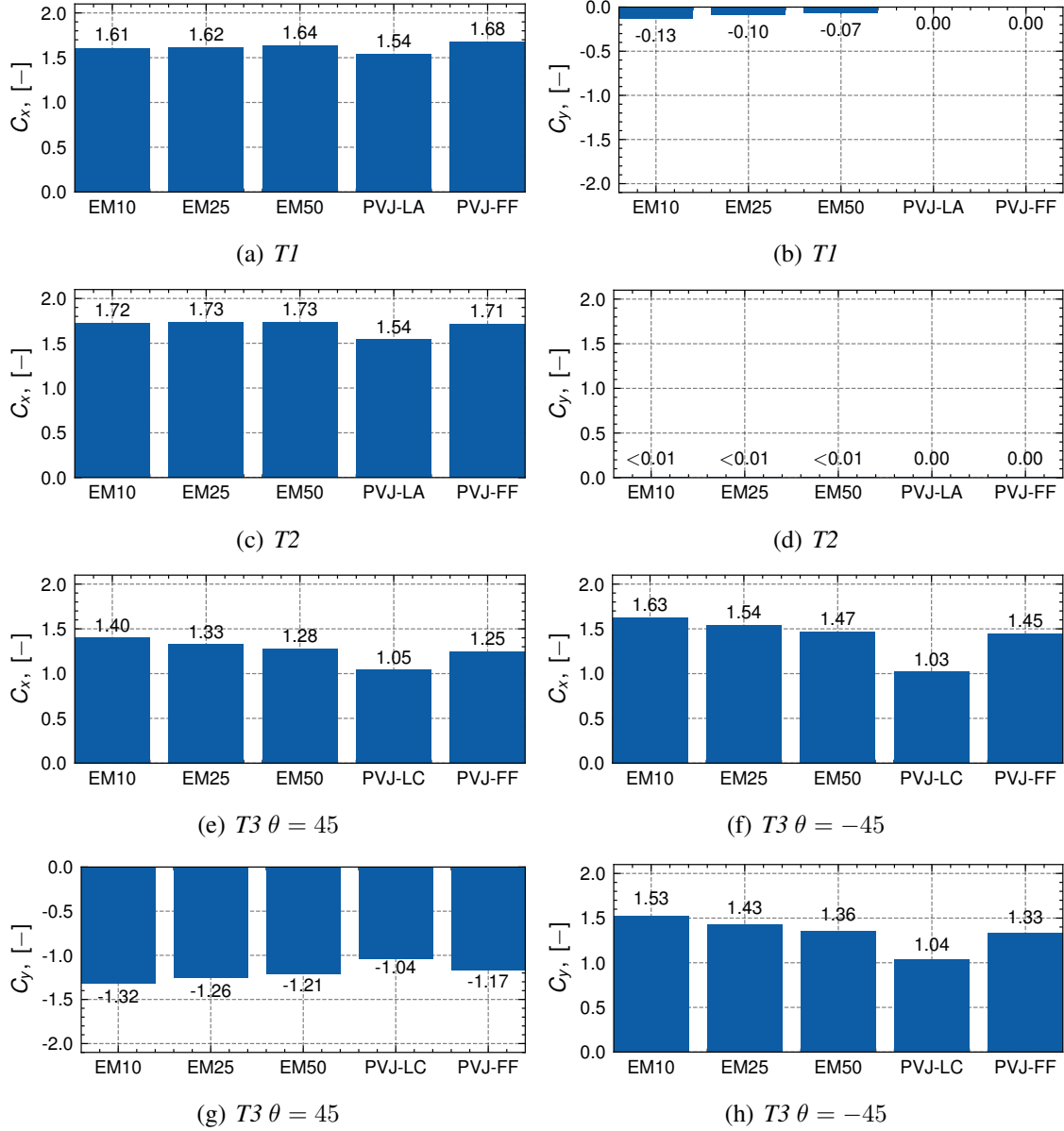
Figure 21: The global aerodynamic coefficients of the ground-mounted porous barrier.

5. Conclusions

In this paper, we proposed a homogenized approach for the modelling of permeable surfaces in CFD simulations. The approach, denoted as PVJ, is valid in the limit of vanishing pore size with respect to the overall studied structure dimensions, and generalises the well-known pressure-jump approach, commonly used for internal flows. In particular, aerodynamic forces exchanged both along the permeable surface normal and tangential directions are considered, leading to a pressure and a tangential velocity jump, respectively. Similarities between the proposed approach and those

based on distributed momentum sources, following the Darcy-Forchheimer modelling for porous media, are discussed.

Firstly, for the sake of generality, the model is introduced relying on a Fourier series expansion of the aerodynamic coefficients with the angle of attack. Then, it is shown that, for particular limit cases, the number of coefficients appearing in the model can be drastically reduced and their value obtained from analytical or semi-analytical considerations.

Finally, the approach is applied in order to model the flow around a ground mounted permeable barrier. In particular, results obtained simulating explicitly the barrier detailed geometry (i.e. modelling all the pores) and adopting the proposed approach, are compared. The coefficients appearing in the *PVJ* model are calculated both by fitting data obtained from an elementary permeable surface element and using the established limit cases. The comparison is performed considering permeable surfaces typologies characterized by very different aerodynamic behaviour, so inducing large differences in the flow field organization downstream the barrier.

The proposed *PVJ* approach is found to well-reproduce the results obtained by the detailed geometrical models, leading to a great simplification of the analysis setup and very large savings in terms of computational costs. The approach is expected to be extremely convenient when a strong scale separation between the pores and the overall structure exists, so allowing to study cases which cannot be simulated using explicit geometrical models. The proposed approach is expected to be extremely particularly indicated for parametric studies and optimizations involving the variation of the permeable surfaces geometry and location.

References

Allori, D., Bartoli, G., Mannini, C., 2013. Wind tunnel tests on macro-porous structural elements: A scaling procedure. Journal of Wind Engineering and Industrial Aerodynamics 123, 291–299.

Annand, W., 1953. The resistance to air flow of wire gauzes. The Aeronautical Journal 57, 141–146.

Azizi, F., 2019. On the pressure drop of fluids through woven screen meshes. Chemical engineering science 207, 464–478.

Basnet, K., 2015. Flow around porous barriers: fundamental flow physics and applications. The University of Iowa.

Belloli, M., Rosa, L., Zasso, A., 2014. Wind loads and vortex shedding analysis on the effects of the porosity on a high slender tower. Journal of Wind Engineering and Industrial Aerodynamics 126, 75–86.

Bruno, L., Horvat, M., Raffaele, L., 2018. Windblown sand along railway infrastructures: A review of challenges and mitigation measures. Journal of Wind Engineering and Industrial Aerodynamics 177, 340–365.

Buljac, A., Kozmar, H., Pospíšil, S., Macháček, M., 2017. Flutter and galloping of cable-supported bridges with porous wind barriers. Journal of Wind Engineering and Industrial Aerodynamics 171, 304–318.

Cao, J., Gao, H., Dou, L., Zhang, M., Li, T., 2019. Modeling flow in anisotropic porous medium with full permeability tensor, in: Journal of Physics: Conference Series, IOP Publishing. p. 012054.

Chen, H., Christensen, E.D., 2016. Investigations on the porous resistance coefficients for fishing net structures. Journal of Fluids and Structures 65, 76–107.

Darcy, H., 1856. Les fontaines publiques de la ville de Dijon: Exposition et application des principes à suivre et des formules à employer dans les questions de distribution d'eau: Ouvrage terminé par un appendice relatif aux fournitures d'eau de plusieurs villes, au filtrage des eaux et à la fabrication des tuyaux de fonte, de plomb, de tôle et de bitume. volume 2. V. Dalmont.

Eckert, B., Pfluger, F., 1942. The resistance coefficient of commercial round wire grids. Technical Report.

Feichtner, A., Mackay, E., Tabor, G., Thies, P.R., Johanning, L., 2021. Comparison of macro-scale porosity implementations for cfd modelling of wave interaction with thin porous structures. Journal of Marine Science and Engineering 9, 150.

Forchheimer, P., 1901. Wasserbewegung durch boden. Z. Ver. Deutsch, Ing. 45, 1782–1788.

Hu, G., Hassanli, S., Kwok, K.C., Tse, K.T., 2017. Wind-induced responses of a tall building with a double-skin façade system. Journal of Wind Engineering and Industrial Aerodynamics 168, 91–100.

Hu, G., Song, J., Hassanli, S., Ong, R., Kwok, K.C., 2019. The effects of a double-skin façade on the cladding pressure around a tall building. Journal of Wind Engineering and Industrial Aerodynamics 191, 239–251.

Kemper, F., Feldmann, M., 2019. Wind load assumptions for permeable cladding elements considering the installation context. Journal of Wind Engineering and Industrial Aerodynamics 184, 277–288.

Kozmar, H., Procino, L., Borsani, A., Bartoli, G., 2014. Optimizing height porous wind barriersand porosity of roadway wind barriers for viaducts and bridges. Engineering Structures 81, 49–61.

Lo, Y.L., Wu, Y.T., Fu, C.L., Yu, Y.C., 2020. Wind load reduction effects on inner buildings by exterior porous façades. Building and Environment 183, 107148.

Maruyama, T., 2008. Large eddy simulation of turbulent flow around a windbreak. Journal of Wind Engineering and Industrial Aerodynamics 96, 1998–2006.

Menter, F.R., Kuntz, M., Langtry, R., 2003. Ten years of industrial experience with the sst turbulence model. Turbulence, heat and mass transfer 4, 625–632.

Miguel, A., Van de Braak, N., Bot, G., 1997. Analysis of the airflow characteristics of greenhouse screening materials. Journal of Agricultural Engineering Research 67, 105–112.

Ooi, C., Chiu, P.H., Raghavan, V., Wan, S., Poh, H.J., 2019. Porous media representation of louvers in building simulations for natural ventilation. Journal of Building Performance Simulation 12, 494–503.

Park, C.W., Lee, S.J., 2003. Experimental study on surface pressure and flow structure around a triangular prism located behind a porous fence. Journal of wind engineering and industrial aerodynamics 91, 165–184.

Patton, E.G., Shaw, R.H., Judd, M.J., Raupach, M.R., 1998. Large-eddy simulation of windbreak flow. Boundary-Layer Meteorology 87, 275–307.

Pomaranzi, G., Bistoni, O., Schito, P., Zasso, A., 2021. Numerical modelling of three-dimensional screens, treated as porous media. Wind and Structures 33, 409–422.

Raffaele, L., van Beeck, J., Bruno, L., 2021. Wind-sand tunnel testing of surface-mounted obstacles: Similarity requirements and a case study on a sand mitigation measure. Journal of Wind Engineering and Industrial Aerodynamics 214, 104653.

Safer, N., Woloszyn, M., Roux, J.J., 2005. Three-dimensional simulation with a cfd tool of the airflow phenomena in single floor double-skin facade equipped with a venetian blind. Solar Energy 79, 193–203.

Taylor, G.I., 1944. The aerodynamics of porous sheets. Aeronautical Reseach Council, Reports and Memoranda 2237, 163–176.

Teitel, M., 2010. Using computational fluid dynamics simulations to determine pressure drops on woven screens. Biosystems engineering 105, 172–179.

Teitel, M., Dvorkin, D., Haim, Y., Tanny, J., Seginer, I., 2009. Comparison of measured and simulated flow through screens: Effects of screen inclination and porosity. Biosystems Engineering 104, 404–416.

Tominaga, Y., Shirzadi, M., 2022. Rans cfd modeling of the flow around a thin windbreak fence with various porosities: Validation using wind tunnel measurements. Journal of Wind Engineering and Industrial Aerodynamics 230, 105176.

Weller, H., 2012. Controlling the computational modes of the arbitrarily structured c grid. Monthly Weather Review 140, 3220–3234.

Wieghardt, K., 1953. On the resistance of screens. Aeronautical Quarterly 4, 186–192.

Xu, M., Patruno, L., Lo, Y.L., de Miranda, S., 2020. On the use of the pressure jump approach for the simulation of separated external flows around porous structures: A forward facing step. Journal of Wind Engineering and Industrial Aerodynamics 207, 104377.

Xu, M., Patruno, L., Lo, Y.L., de Miranda, S., 2022a. Simulation strategies for wind shields and porous barriers for bridge deck optimization, in: Structures, Elsevier. pp. 824–839.

Xu, M., Patruno, L., Lo, Y.L., de Miranda, S., Ubertini, F., 2022b. On the numerical simulation of perforated bluff-bodies: a cfd study on a hollow porous 5: 1 rectangular cylinder. Wind and Structures 34, 1–14.

Xu, M., Patruno, L., Lo, Y.L., de Miranda, S., Ubertini, F., 2022c. Simulation of porous claddings using les and urans: A 5:1 rectangular cylinder. Wind and Structures 35, 67–81.

Yang, J., Lee, S., 1999. Effect of anisotropy on transport phenomena in anisotropic porous media. international Journal of Heat and Mass transfer 42, 2673–2681.